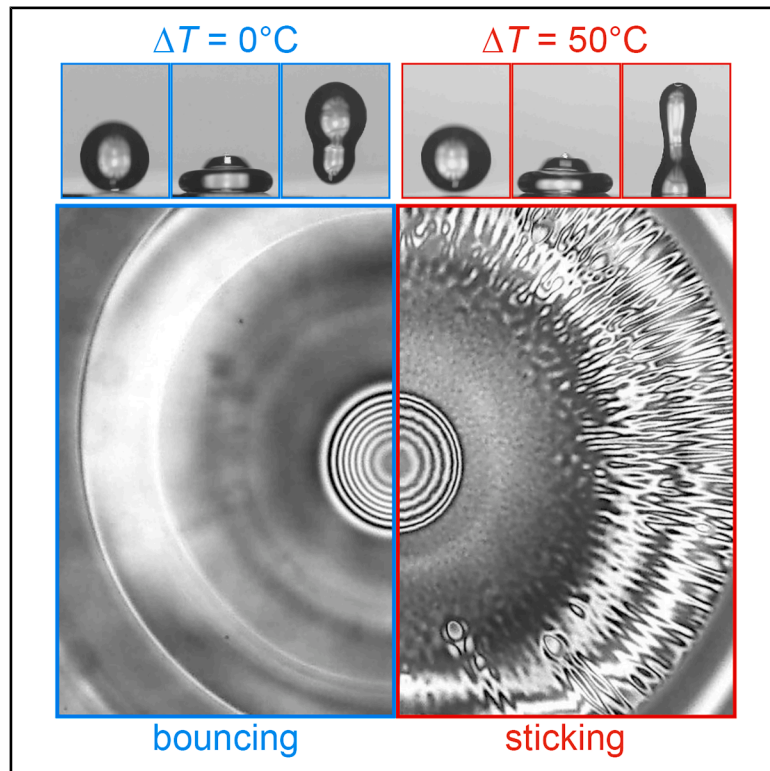


Condensation-induced roughness controls non-contact bouncing of hot drops

Graphical abstract



Authors

Guillaume Deschasaux, Sakura Torii, Jiaying Shen, Yuki Serata, Pritam Kumar Roy, Mizuki Tenjimbayashi, Timothée Mouterde

Correspondence

mouterde@g.ecc.u-tokyo.ac.jp

In brief

Drops impacting smooth surfaces can rebound without ever touching them, cushioned by a thin air film. Deschasaux et al. show that this non-contact bouncing fails for hot water drops on colder lubricated surfaces because vapor condenses within the air film, forming liquid roughness that triggers contact. High-speed interferometry experiments and modeling reveal that condensation and heat transfer set the bouncing threshold, clarifying how temperature differences control wetting in air-film-mediated impacts and offering design rules for manipulating droplets.

Highlights

- Non-contact bouncing is lost for hot water drops on colder substrates
- Condensation on the substrate creates liquid roughness that triggers contact
- Low-volatility drops keep bouncing, confirming the role of condensation
- Mass and heat transfer model predicts critical bouncing velocities and rupture times

Article

Condensation-induced roughness controls non-contact bouncing of hot drops

Guillaume Deschasaux,¹ Sakura Torii,¹ Jiaying Shen,¹ Yuki Serata,¹ Pritam Kumar Roy,^{1,2} Mizuki Tenjimbayashi,³ and Timothée Mouterde^{1,4,5,*}

¹Department of Mechanical Engineering, School of Engineering, The University of Tokyo, Tokyo, Japan

²Department of Physics, Central University of Rajasthan, Rajasthan, India

³Research Center for Materials Nanoarchitectonics (MANA), National Institute for Materials Science (NIMS), Ibaraki, Japan

⁴Senior author

⁵Lead contact

*Correspondence: mouterde@g.ecc.u-tokyo.ac.jp

<https://doi.org/10.1016/j.newton.2026.100587>

ACCESSIBLE OVERVIEW Droplets impacting sufficiently smooth surfaces can bounce without ever touching the substrate. In this non-contact bouncing regime, the droplet is supported by a thin air film, which prevents wetting throughout rebound. Beyond its fundamental interest, this property does not depend on how well a liquid wets the surface, making it relevant to applications where controlling rebound matters. Lubricant-coated surfaces provide a robust way of obtaining non-contact bouncing, as the coating forms a smooth interface and can bury small defects or dust particles. Although non-contact bouncing is well understood under isothermal conditions, its robustness when the drop and surface have different temperatures remains unclear. Here, we show that hot water drops impacting a cooler lubricated surface lose their ability to bounce as the temperature difference increases. The maximum impact speed allowing rebound decreases, and drops that would bounce under isothermal conditions instead contact the lubricant and spread. Using high-speed imaging and interferometry, we directly observe the air film beneath the drop and identify the origin of this transition. The hot drop is surrounded by warm, vapor-rich air, from which water vapor rapidly condenses on the colder lubricant surface. These microscopic condensates form a liquid roughness within the air film. When this roughness grows large enough to bridge the remaining gap between the drop and the lubricant, contact is triggered, and bouncing fails. The effect disappears for low-volatility liquids such as silicone oil, showing that the transition is caused by evaporation and condensation rather than by temperature alone. We also develop a model coupling impact dynamics, condensation growth, and heat transfer, which predicts both the bouncing threshold and the time at which contact occurs. These results reveal that non-contact bouncing is controlled not only by impact speed and surface smoothness but also by volatility and thermal transport.

SUMMARY

Droplets impacting smooth substrates can bounce without contact, as a gas film dynamically prevents wetting, provided the impact velocity remains below the threshold at which gas-kinetic effects and van der Waals interactions trigger contact. For hot droplets, however, condensation within this air film can destabilize the non-contact state. Here, we investigate the impact of hot water droplets on lubricant-infused surfaces, with the droplets initially hotter than the substrate by ΔT . High-speed imaging and interferometry reveal that the maximum bouncing velocity decreases with ΔT due to rapid condensation growth (~ 1 ms) on the lubricant layer, which generates a liquid roughness that triggers the contact. This phenomenon vanishes for low-volatility liquids. Our model, coupling condensation dynamics and thermal transfer, quantitatively predicts the critical bouncing velocity and the condensation bridging time. It also shows that the transition depends on the substrate and drop thermal properties, providing a predictive framework for hot-drop impacts in the non-contact bouncing regime.

INTRODUCTION

Droplet impact on a solid surface¹ is common in daily life, yet it is central to many industrial and technological processes ranging from inkjet printing^{2,3} and additive manufacturing⁴ to pesticide deposition,⁵ spray cooling,⁶ drug delivery,⁷ and icing prevention.⁸ Although droplet impacts may appear simple at first glance, advances in imaging techniques have revealed a rich physics governed by the interplay between liquid dynamics, the subjacent gas layer, and interactions with the substrate.^{9,10} Depending on the impact conditions, a drop may spread on the solid,¹¹ splash into multiple droplets,^{12–14} form a jet,^{15,16} trap a gas pocket beneath it,^{17,18} or bounce from the surface.¹⁰

Among these outcomes, bouncing is mainly observed on superhydrophobic surfaces, which are substrates covered with hydrophobic textures.¹⁹ On such surfaces, the drop only comes into contact with the top of the solid textures, which reduces the adhesion, allowing the droplet to bounce and leave the substrate dry. When a temperature difference exists between the drop and the substrate, the picture becomes more complex. For instance, when a hot drop impacts a cooler superhydrophobic surface, condensation can form within the surface textures, forming liquid bridges that increase adhesion and suppress rebound,^{20,21} while texture melting,²² freezing,^{23,24} or solidification²⁵ during impact can have similar effects. In contrast, drop combustion has been reported to enhance bouncing, most likely due to thermocapillary effects.²⁶ The sensitivity of bouncing to such thermally driven phase-change processes depends strongly on the contact time with the substrate,²⁷ which is set by the drop's inertio-capillary timescale²⁸ but can be reduced by introducing surface macrot textures.^{29–31}

While bouncing is robust and readily obtained on superhydrophobic surfaces, it is not limited to them. On hydrophilic or wetted substrates, droplets usually deposit; yet Kolinski³² and de Ruiter³³ showed that droplets can rebound without any direct contact with the substrate. In this non-contact bouncing regime, also sometimes referred to as air-film-mediated bouncing, the drop is entirely supported by a sub-micrometric air film, sustained by lubrication pressure in the surrounding gas, that prevents wetting throughout the impact. This gas layer thickness decreases with increasing impact velocity and remains stable down to thicknesses of a few tens of nanometers,³⁴ below which van der Waals forces trigger contact.³⁵ Achieving this regime is challenging and requires substrates of exceptional smoothness. This condition is more easily obtained with lubricated surfaces than with dry ones, as dust particles tend to sink into the lubricant, making the surfaces more robust to contamination and thereby enabling the observation and study of non-contact bouncing.^{36–38} While thermal effects and phase-change phenomena have been widely investigated for superhydrophobic surfaces, the case of hot water drops impacting the non-contact bouncing regime remains essentially unexplored and is the object of the present study.

RESULTS

Hot-drop impact experiments

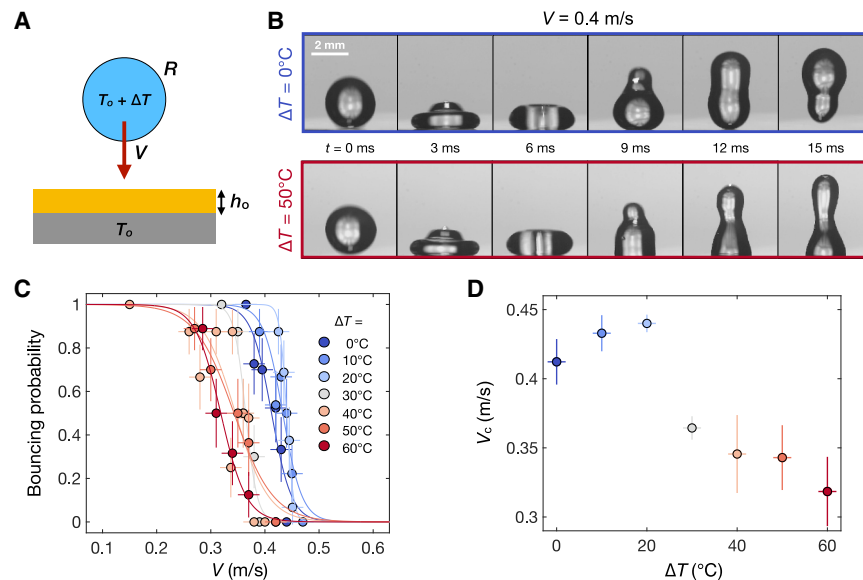
Water droplets with radius $R = 1.3 \pm 0.1$ mm, density $\rho = 1,000$ kg/m³, and surface tension $\gamma = 72$ mN/m are dropped on

a lubricant-infused non-textured surface³⁹ coated with a layer of silicone oil (X-22-170BX, ShinEtsu Chemical; viscosity: $\eta = 39$ mPa.s, density: $\rho_L = 970$ kg/m³) of thickness $h_o = 8 \pm 1$ μ m (see [methods](#) section [substrate preparation](#)). The experiments are conducted with a relative humidity $RH \approx 60\% \pm 2\%$, and the surface is initially at room temperature $T_o = 25^\circ\text{C} \pm 1^\circ\text{C}$, while the droplet temperature $T_o + \Delta T$ is set by a droplet dispenser (ML6000X, Musashi Engineering) so that the temperature difference between the droplet and the surface ΔT can be varied from 0°C to 60°C ([Figure 1A](#)). The impact velocity V , determined using side-view high-speed imaging (MEMREMCAM HX-7, NAC), is varied by adjusting the release height of the droplet. We first observe impacts of water droplets with velocity $V = 0.4$ m/s and temperature difference $\Delta T = 0^\circ\text{C}$ and 50°C , respectively. Snapshots of both impacts are shown in [Figure 1B](#), with each frame separated by 3 ms. Without temperature difference, $\Delta T = 0^\circ\text{C}$, the droplet bounces on the surface with a total apparent contact time of around 12 ms, a duration that matches the inertio-capillary contact time τ of drops bouncing on superhydrophobic surfaces $\tau \approx 2.5 (\rho R^3/\gamma)^{1/2}$.^{28,36} For $\Delta T = 50^\circ\text{C}$ ([Figure 1B](#), bottom row), the droplet comes into contact with the surface after ~ 6 ms, which prevents bouncing despite impacting the substrate with the same Weber number $We = \rho V^2 R/\gamma$ ($We \approx 3$) as the isothermal case. This bouncing temperature-induced transition is outside the scope of current non-contact droplet-bouncing models, as bouncing failure is typically attributed to variations in the Weber, Reynolds, and Stokes numbers⁴⁰ and indicates the presence of an underlying phenomenon that we further investigate.

We quantify the effect of temperature differences on the bouncing transition by systematically varying both ΔT from 0°C to 60°C and the impact velocity from 0.15 to 0.5 m/s, a velocity range for which the bouncing transition is observed. For each value of ΔT and V , we perform 10 impact experiments, and we count the number of successful rebounds to determine the bouncing probability. [Figure 1C](#) shows the bouncing probability as a function of V color coded from blue to red for ΔT varying from 0°C to 60°C . This graph reveals two key observations: (1) for all temperature differences, the probability varies from 1 to 0 when the velocity becomes larger than a critical value V_c . (2) The critical velocity at which the transition occurs is lower for large temperature differences ΔT . To more precisely characterize the transition velocity, for each ΔT , we fit the probability data with a sigmoid function $p = 0.5 - 0.5 \tanh((V - V_c)/\Delta V)$, where V_c is the transition velocity and ΔV the steepness (fits are shown with plain lines in [Figure 1C](#)). The evolution of V_c with ΔT plotted in [Figure 1D](#) reveals two regimes: for $\Delta T < 25^\circ\text{C} \pm 5^\circ\text{C}$, the bouncing velocity first slightly increases before sharply decreasing from ~ 0.45 to ~ 0.35 m/s when ΔT becomes larger than $\sim 25^\circ\text{C}$ to reach a second regime ($\Delta T > 25^\circ\text{C} \pm 5^\circ\text{C}$) where the critical velocity then slowly decreases with ΔT to reach 0.32 m/s for $\Delta T = 60^\circ\text{C}$. We now investigate the origin of this temperature-induced bouncing transition.

Reflection interference contrast microscopy

Non-contact bouncing arises from the air film formed between the droplet and the substrate, which slows down and reverses the momentum of the droplet. To understand the bouncing



50%. Horizontal error bars indicate the estimated experimental uncertainty on the initial temperature difference. Vertical error bars represent the 95% confidence interval of the fitted transition velocity V_c .

failure at large temperature differences, we use reflection interference contrast microscopy (RICM) to directly observe the interference pattern formed by light reflected on the oil-air and air-water interfaces (Figure 2A). In brief, an inverted microscope (IX-73, Olympus) is equipped with a $5\times$ objective lens, the surface and droplet are illuminated with a LED monochromatic light (M455L4-C5, Thorlabs; wavelength $\lambda = 455 \text{ nm}$, bandwidth $\Delta\lambda \approx 18 \text{ nm}$), and the interference pattern is captured using a high-speed camera (Nova Fastcam S6, Photron) at 10 kHz . The intensity varies with $\cos(4\pi\delta/\lambda)$, with $\delta(r, t)$ representing the local thickness of the air film, so that adjacent black and white fringes correspond to a height variation of the air film of $\lambda/4$ – 108 nm , which allows for precise measurements of film thickness.

The time evolution of the interference patterns of droplets with impact velocity $V = 0.4 \text{ m/s}$ ($We \approx 2.9$) with temperature differences $\Delta T = 0^\circ\text{C}$ (bouncing), 30°C , and 50°C (non-bouncing) is shown in Figure 2B. We take the origin of time ($t = 0$) as the moment when the first fringes appear on the interferogram, which corresponds to the droplet being at half the coherence length $L \approx (2\ln 2/\pi)\lambda^2/\Delta\lambda$ from the substrate, which is around $L/2 \approx 3 \mu\text{m}$. The time step in Figure 2B is selected to display the full bouncing behavior ($\Delta T = 0^\circ\text{C}$) or, for conditions leading to coalescence ($\Delta T = 30^\circ\text{C}$ and 50°C), just until the droplet merges with the oil.

The snapshots (Videos S1, S2, S3, S4, and S5) reveal very distinct interferogram patterns, which correspond to the two critical velocity regimes observed in Figure 1C. In the isothermal case, $\Delta T = 0^\circ\text{C}$ (Figure 2B, left), we observe the fringe pattern commonly reported in the literature^{32–38}: a central dimple expands as time advances before the droplet retracts, leaving the substrates after the typical inertio-capillary time τ . However, for $\Delta T = 30^\circ\text{C}$ and 50°C (Figure 2B, middle and right), we observe

a new regime characterized by an unusual interferogram in which micrometric circular patterns appear. We believe these marks to be condensation droplets nucleating on the lubricant layer, the shape of which slightly reduces the distance between the substrate and the droplet interface, thereby appearing in the interference pattern. Qualitatively, near the hot impacting drop, the atmosphere is saturated with water vapor at a concentration $c_{\text{sat}}(T_o + \Delta T)$ that exceeds the saturated vapor concentration $c_{\text{sat}}(T_o)$ of the lubricant initially at temperature T_o . Due to this supersaturated atmosphere, heterogeneous nucleation occurs on the lubricant layer. Denoting $\Delta c_{\text{sat}} = c_{\text{sat}}(T_o + \Delta T) - c_{\text{sat}}(T_o)$ and δ as the typical thickness of the air layer, condensation droplets then grow due to a diffusive flux $D\Delta c_{\text{sat}}/\delta$, where $D \approx 25 \text{ mm}^2/\text{s}$ is the water vapor diffusion coefficient in air. A close look at the interference patterns (Figures 2B and 2C) reveals at least three features that support the condensation hypothesis: (1) increasing ΔT increases the nucleation density (see Figure S1), consistent with classical nucleation theory, as it leads to higher supersaturation and thus greater nucleation rates. (2) The growth rate of the condensation drops can be estimated from the interference pattern. The typical number of fringes of condensation droplets increases from 2 to 4 within 1 ms for $\Delta T = 30^\circ\text{C}$ and 0.5 ms for $\Delta T = 50^\circ\text{C}$. This corresponds to a height variation of $\lambda/2$ – 200 nm , which gives a condensation growth velocity increasing from 0.3 to 0.6 mm/s when increasing ΔT from 30°C to 50°C . This further supports the condensation hypothesis, as larger ΔT increases the diffusive flux. (3) The kink region, where the air layer thickness δ is the smallest, corresponds to the location of the tallest condensation droplets. This agrees well with a condensation growth due to a diffusive flux $D\Delta c_{\text{sat}}/\delta$, which is inversely proportional to the local thickness.

Most importantly for the impacting droplet's fate, condensation forms a liquid roughness that initiates the contact between

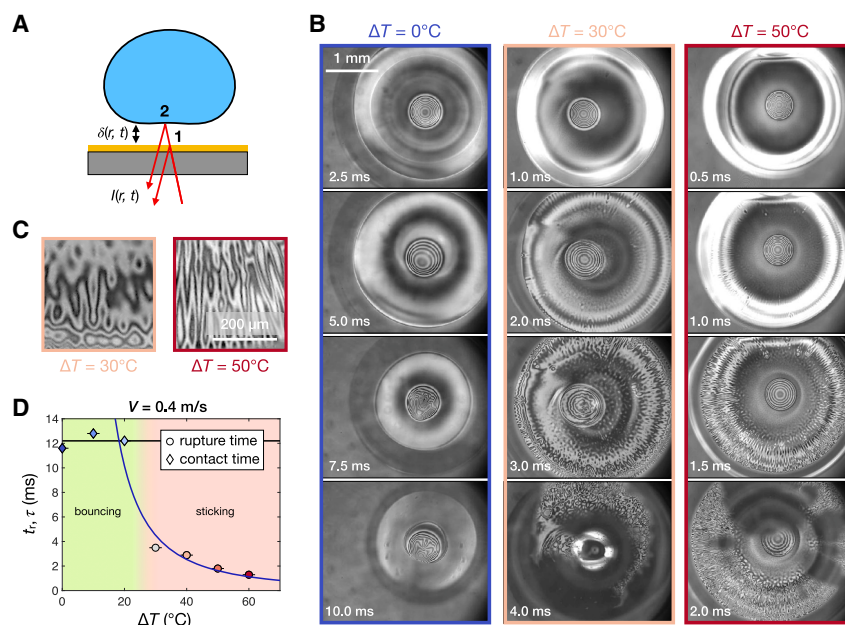


Figure 2. Reflection interference contrast microscopy experiments

(A) Schematic view of the reflection interference contrast microscopy (RICM) setup. A collimated beam of monochromatic light is reflected by the lubricant-air and air-droplet interfaces. The two beams interfere, and the resulting fringe pattern is captured using a microscope with a high-speed camera recording at 10,000 fps. The interferograms depend on the optical path difference $2\delta(r, t)$ between the two beams, thus giving a measurement of the air layer thickness.

(B) Time evolution of the interference patterns obtained by RICM for water droplets impacting velocity $V = 0.4$ m/s and $\Delta T = 0, 30^\circ\text{C}$ and 50°C . Scale bar: 1 mm.

(C) Detail of RICM images of condensation close to the droplet edge for $\Delta T = 30^\circ\text{C}$ and 50°C at times 3.0 and 1.5 ms, respectively.

(D) Evolution of the rupture time t_r (circles) and the contact time τ (diamonds) with ΔT for droplets with velocity $V = 0.4$ m/s. The blue line shows the prediction for the rupture time of Equation 7, and the black line corresponds to $\tau \approx 2.5 (\rho R^2/\eta)^{1/2}$ with $R \approx 1.2$ mm. Marker colors match those in Figures 1C and 1D and represent temperature.

The green- and pink-shaded areas denote the bouncing and sticking regimes, respectively. Horizontal and vertical error bars indicate the estimated experimental uncertainty in the initial temperature difference and time measurements, respectively.

the droplet and the lubricant layer after a time t_r . The contact appears in the high-speed interferograms as a darkened area (last frames of Figure 2B for $\Delta T = 30^\circ\text{C}$ and 50°C), which allows us to measure and plot t_r as a function of ΔT in Figure 2D (circles). This time decreases from ~ 4 to 1 ms as ΔT increases from 30°C to 60°C , a sign that the condensation-induced liquid roughness grows faster with larger ΔT . We note that, within the range of impact velocities explored here, any occurrence of contact consistently prevents bouncing. In the bouncing case, we plot the apparent contact time (diamonds, Figure 2B), which we measure from appearance to disappearance of the interference pattern.

To verify our hypothesis that the interference pattern and rupture mechanism are related to water condensation on the lubricant layer and do not arise from purely temperature-related effects, we perform the same experiment but with silicone oil droplets (X-22-170BX, ShinEtsu Chemical) with $R = 0.8 \pm 0.1$ mm. Unlike water, this liquid is non-volatile, so we expect all evaporation/condensation mechanisms to be suppressed. We first observe the interference pattern for impacting velocity $V = 0.45$ m/s, with $\Delta T = 0^\circ\text{C}$ and 60°C (Figure 3A). In contrast to the water case, with silicone oil there is no difference between the isothermal and hot cases, and the interferogram resembles that of the isothermal water case where condensation does not occur. It confirms that the pattern observed for hot water drops is condensation.

To further validate that condensation is also at the origin of the non-bouncing transition, we measure and plot in Figure 3B the bouncing probability of silicone oil drops, as a function of their impact velocity V and for ΔT ranging from 0°C to 60°C . These curves reveal that, with silicone oil, the bouncing probability becomes nearly independent of ΔT , with a transition to non-bounc-

ing for $V_c \approx 0.45 \pm 0.03$ m/s. The difference in behavior between volatile (water) and non-volatile (silicone oil) liquids is made more obvious in Figure 3C, where we plot the critical transition velocity V_c , normalized by its isothermal value $V_{c,0} = V_c(\Delta T = 0^\circ\text{C})$, as a function of ΔT for both water and silicone oil. For silicone oil, $V_c/V_{c,0}$ remains close to unity and decreases only slightly with ΔT . By contrast, water exhibits a non-monotonic variation, with a slight increase of the threshold at low ΔT , followed by a sharp decrease beyond $\Delta T = 20^\circ\text{C}$ – 30°C , highlighting the marked difference between volatile and non-volatile liquids. The initial increase may originate from a Marangoni effect described by Geri⁴¹ and Liu²⁶: during impact, the center of the hot drop closer to the colder substrate cools more rapidly than the sides, creating an inward Marangoni flow that thickens the air layer, thereby stabilizing the non-contact state and slightly increasing the critical velocity. This effect is controlled by the Marangoni number that decreases as $1/\eta$, so it should be strongly damped for silicone oil, whose viscosity is about 40 times higher than that of water.⁴¹ In that case, the gradual decrease of the critical velocity may be explained by the reduction of the surface tension with increasing temperature. Assuming that the non-bouncing transition is governed by a critical We ,⁴⁰ $We_c = \rho V_c^2 R/\gamma$, and denoting $\Gamma = d\gamma/dT$ as the thermal coefficient of surface tension so that $\gamma(\Delta T) = \gamma_0 + \Gamma\Delta T$, we expect the velocity ratio to decrease with $V_c/V_{c,0} \approx (1 + \Gamma\Delta T/\gamma_0)^{1/2}$. Taking $\gamma_0 \approx 20$ mN/m and $\Gamma \approx -0.043$ mN/K (Figure S2), we get $V_c/V_{c,0}(\Delta T = 0^\circ\text{C})$ around 0.93 for $\Delta T = 60^\circ\text{C}$, in good agreement with the experimental data (Figure 3C). We now model the sharp decrease in critical velocity observed in water at larger ΔT , which cannot be accounted for by thermocapillary effects or surface tension decreases but rather originates from evaporation-condensation processes.

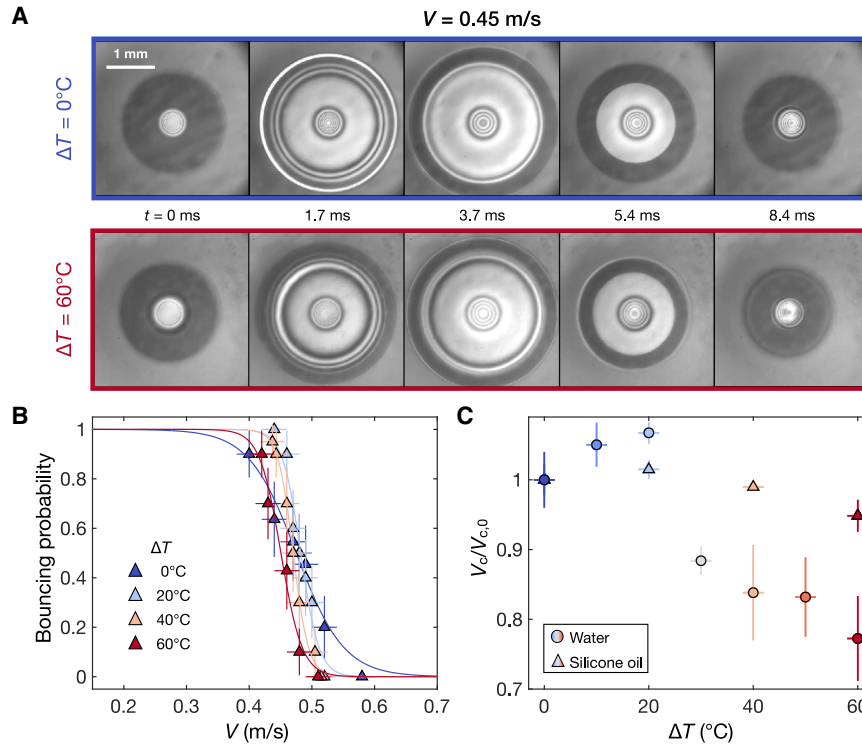


Figure 3. Non-volatile liquid bouncing experiments

(A) Time evolution of the interference patterns obtained by RCM for silicone oil drops ($R = 0.8 \text{ mm}$) with impacting velocity $V = 0.45 \text{ m/s}$ and $\Delta T = 0^\circ\text{C}$ and 60°C . Scale bar: 1 mm .

(B) Bouncing probability of silicone oil droplets impacting the substrate plotted as a function of impact speed V for different ΔT . The bouncing transition is fitted with a sigmoid $p = 0.5 - 0.5 \tanh((V - V_c)/\Delta V)$. Horizontal error bars indicate the estimated experimental uncertainty in the impact velocity, and the vertical error bars indicate the binomial standard error of the bouncing probability, estimated from ($n = 10$) repeated impacts as $\sigma_p = \sqrt{p(1-p)/n}$, where p is the measured bouncing probability.

(C) V_c , normalized by $V_{c,0}$, its value for $\Delta T = 0^\circ\text{C}$, plotted as a function of ΔT for water (circles) and silicone oil (triangles). Horizontal error bars indicate the estimated experimental uncertainty on the initial temperature difference. Vertical error bars represent the 95% confidence interval of the fitted transition velocity V_c .

Condensation and heat transfer model

To explain our observations, we build a model that incorporates the drop impact dynamics and the heat and mass diffusion to predict the condensation dynamics and ultimately the bouncing or non-bouncing behavior. We assume that the problem is axisymmetric about the central vertical axis of the droplet during impact, and we denote the radial and vertical coordinates as r and z , respectively (Figure 4A). Our model aims to describe condensation growth during impact to predict when the drop contacts the condensation, which prevents bouncing. Instead of describing individual condensation droplets, we consider the theoretical envelope formed by their tops and treat them as a film of height $h(r, t)$ as sketched in Figure 4A. Due to the difference in scale between the air layer thickness $\delta \sim \mu\text{m}$ and its lateral extension $R \sim \text{mm}$, we consider only the vertical gradients ($\partial/\partial z$) and neglect the horizontal ones ($\partial/\partial r$). The difference between the drop's surface temperature $T_{W,S}$ and the lubricant's surface temperature $T_{L,S}$ creates a local water vapor concentration difference $\Delta c_{\text{sat}} = c_{\text{sat}}(T_{W,S}) - c_{\text{sat}}(T_{L,S})$ between the drop and the condensation distant by $H - h$, where H is the distance from the lubricant to the drop bottom interface. When the droplet approaches the surface, a vapor-rich layer develops next to its bottom interface, with a typical thickness ℓ that can be estimated by balancing diffusive transport across the layer with advection renewal due to the droplet velocity V . This corresponds to a Péclet number $\text{Pe} = \ell V/D \sim 1$, which gives $\ell \sim D/V$. With $D \sim 10^{-5} \text{ m}^2/\text{s}$ and $V \sim 1 \text{ m/s}$, we obtain $\ell \sim 10 \mu\text{m}$. The diffusion time for the concentration gradient to be established scales as ℓ^2/D , that is $\sim 10 \mu\text{s}$ for $\ell \sim 10 \mu\text{m}$. This time is much shorter than the characteristic timescale over which the air layer thickness

evolves during bouncing and rupture events, as observed in Figure 2D ($\sim 5\text{--}10 \text{ ms}$). Therefore, we assume a quasi-steady state for the vapor concentration profile in the air layer, so that the diffusive flux that controls the condensation growth is written as $D\Delta c_{\text{sat}}/(H - h)$, and the mass conservation equation is written as

$$\frac{\partial h}{\partial t} = a \frac{D}{\rho} \frac{\Delta c_{\text{sat}}}{H - h}, \quad (\text{Equation 1})$$

where a is an adjustable parameter of order one that accounts for the shape of condensation drops on the lubricant layer, which will be discussed later. To solve this equation, we need to consider both the drop dynamics and thermal transport, as they control the time variations of H and Δc_{sat} , respectively. We estimate $H(r, t)$ during the spreading phase, when contact is experimentally observed, for different impact velocities by numerically solving the complete 2D incompressible Navier-Stokes equations using the open-source solver *Basilisk*^{42,43} (see Note S3). We also assume that condensation droplets are small enough ($<500 \text{ nm}$; Figure 2B) such that they do not affect the drop dynamics; consequently, the isothermal $H(r, t)$ is used for all ΔT .

The vapor concentration difference Δc_{sat} that drives condensation strongly depends on the temperature difference between the drop and lubricant surfaces. While the initial temperature difference is set to ΔT , heat transfer from the drop to the lubricant reduces the dynamic temperature difference $\Delta T_{\text{dyn}} = T_{W,S} - T_{L,S}$, thereby slowing down condensation growth.

To rationalize these effects, we assume that the condensate layer is thin enough that its thermal resistance can be neglected

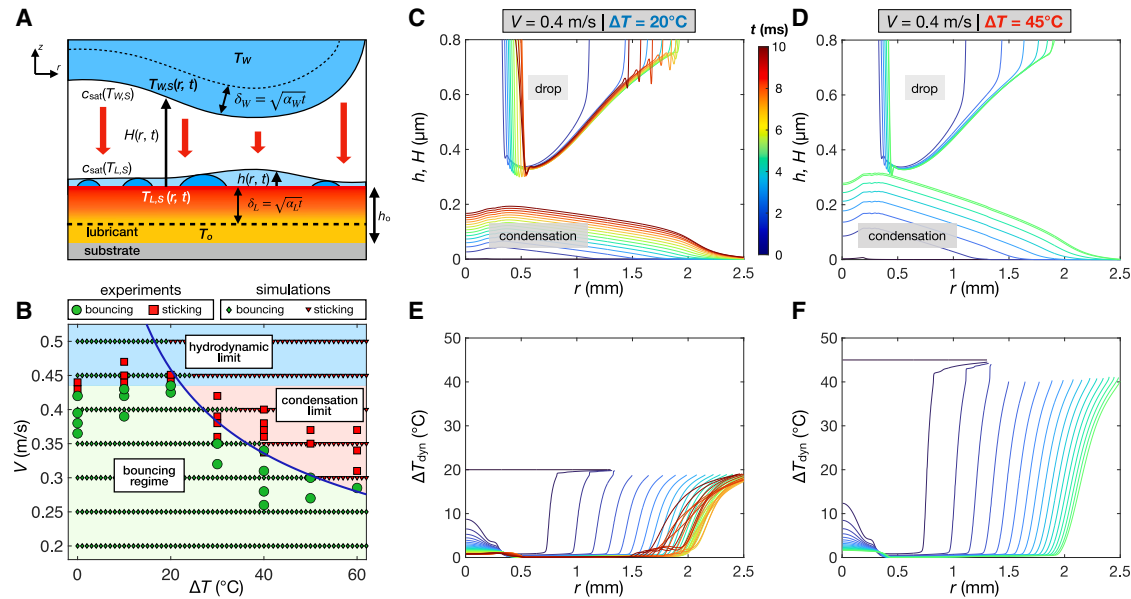


Figure 4. Condensation model and simulation

(A) Sketch of the system considered in our model. The drop at temperature with bulk and surface temperature T_W and $T_{W,S}(r, t)$, respectively, is at a distance $H(r, t)$ from the top of the lubricant layer at temperature $T_{L,S}(r, t)$ on which condensation grows with a height $h(r, t)$. Heat transfer is considered in the drop, the air, and the lubricant layer. Dashed lines delineate the thermal diffusion lengths in the lubricant δ_L and in the water δ_W , and the red arrows indicate vapor flow. Black single- and double-headed arrows denote heights and distances, respectively.

(B) Experimental outcome of the impact as a function of the impact velocity V and the temperature difference ΔT . Bouncing (probability larger than 0.5) is marked with green circles, while spreading (probability lower than 0.5) is marked with red squares. The green diamonds and red triangles show bouncing or spreading, respectively, predicted by the numerical integration. The green-shaded area indicates the bouncing regime; the blue and pink areas represent the sticking regimes governed by hydrodynamic and condensation limits, respectively. The blue line represents the scaling law (Equation 6) of the border between both regimes.

(C and D) Condensation profile h and air layer thickness H as a function of the radial coordinate and plotted at different times, color coded from 0 to 10 ms from blue to red. We show the cases for impact velocity $V = 0.4$ m/s and $\Delta T = 20^\circ\text{C}$ (C) or 45°C (D). Two profiles are separated by $700\ \mu\text{s}$. The top curves in each plot represent the position of the drop interface at different times.

(E and F) Temporal evolution of the radial temperature difference $\Delta T_{\text{dyn}}(r)$, using the same colormap as in (C) and (D). The parameters used here are identical to those in (C) and (D), respectively, except that the two profiles are separated by $250\ \mu\text{s}$.

relative to those of the air and lubricant layers, so that it remains at the lubricant surface temperature $T_{L,S}$. We then consider the heat transfer from the hot drop to the lubricant layer, arising from two mechanisms: heat conduction across the air layer and latent heat release upon condensation. The thermal diffusivity of air α_a is of the same order of magnitude as the mass diffusion coefficient, and the characteristic thermal diffusion time $\delta^2/\alpha_a \sim 5\ \mu\text{s}$ is much shorter than the bouncing and rupture times. We therefore assume a quasi-steady state for the heat transfer in the air layer. Denoting by $\lambda_a \approx 26\ \text{mW}/(\text{m K})$ the air thermal conductivity and by $L_v \approx 2,200\ \text{kJ/kg}$ the latent heat of vaporization, the conductive heat flux is given by $\lambda_a(T_{W,S} - T_{L,S})/(H - h)$, while the latent heat flux is written as $L_v D \Delta c_{\text{sat}}/(H - h)$.

Finally, we assume that heat diffuses into the lubricant layer during a time t over a thermal diffusion length $\delta_L \approx (\alpha_L t)^{1/2}$, with $\alpha_L = \lambda_L/\rho_L c_L$ the lubricant's thermal diffusivity, $\lambda_L \approx 150\ \text{mW}/(\text{m K})$ its thermal conductivity, and $c_L \approx 1,600\ \text{J}/(\text{kg K})$ its specific heat capacity at constant pressure. The corresponding heat flux from the surface to the position δ_L in the lubricant layer is then written as $\lambda_L(T_{L,S} - T_o)/\delta_L$. Similarly, heat diffuses into the drop over a thermal diffusion length $\delta_W \approx (\alpha_W t)^{1/2}$, with $\alpha_W =$

$\lambda_W/\rho_W c_W$, where the water's thermal diffusivity $\lambda_W \approx 600\ \text{mW}/(\text{m K})$ and its specific heat capacity $c_W \approx 4,180\ \text{J}/(\text{kg K})$. The related heat flux extracted from the drop is written as $\lambda_W(T_W - T_{W,S})/\delta_W$.

Heat flux continuity across the drop/air/lubricant interfaces is then written by

$$\begin{aligned} \lambda_W \frac{T_W - T_{W,S}}{\sqrt{\alpha_W t}} &= \lambda_a \frac{T_{W,S} - T_{L,S}}{H - h} + L_v D \frac{c_{\text{sat}}(T_{W,S}) - c_{\text{sat}}(T_{L,S})}{H - h} \\ &= \lambda_L \frac{T_{L,S} - T_o}{\sqrt{\alpha_L t}} \end{aligned}$$

These coupled equations are solved using a finite difference scheme with a time step of $\Delta t = 10\ \mu\text{s}$, matching the Basilisk simulations, and a spatial resolution of $\Delta r = 2.5\ \mu\text{m}$. At each time step, the coupled evolution of the condensation height $h(r, t)$ and the surface temperatures $T_{W,S}(r, t)$ and $T_{L,S}(r, t)$ are solved iteratively. The saturated water vapor concentration is estimated using the Rankine formula (see [methods](#) section [saturated vapor concentration](#)). The simulation stops in two cases. (1) Non-bouncing case: condensation grows fast enough to contact the drop so that at a position r_o and time t_r , $H(r_o, t_r) = h(r_o, t_r)$. (2) Bouncing case: during the entire bouncing event ($\sim 10\ \text{ms}$),

the condensation height remains smaller than the air layer thickness, $h(r, t) < H(r, t)$.

To test our model, the measured bouncing probability p of Figure 1D is displayed on a V - ΔT diagram and marked with green circles for bouncing ($p > 0.5$) and red squares for sticking ($p \leq 0.5$). On the same diagram, we also plot the outcome predicted by our model obtained using the only adjustable parameter of Equation 1, a , set to 0.38. Bouncing cases are marked with green diamonds, while red triangles represent sticking cases.

We find that for impact velocities below 0.45 m/s, our model is in very good agreement with the experimental data, as it reproduces the loss of bouncing observed for $\Delta T > 25^\circ\text{C}$ and the decrease of the maximum bouncing velocity, which drops around 0.3 m/s for $\Delta T = 60^\circ\text{C}$, both for the experiments and the model. Experimentally, for velocities above 0.45 m/s, the drop never bounces, even in the isothermal case. This regime, denoted as a hydrodynamic limit on the diagram, corresponds to sufficiently large impact velocities for which the air layer thins to nanometric thicknesses. At this stage, gas-kinetic effects become important, and van der Waals interactions trigger air-film rupture and suppress rebound.^{32–38} Our model does not aim at predicting this boundary, hence the apparent discrepancy here.

The model also predicts the evolution of the condensation height $h(r, t)$, which we plot for $V = 0.4$ m/s in a bouncing ($\Delta T = 20^\circ\text{C}$, Figure 4C) and a non-bouncing ($\Delta T = 45^\circ\text{C}$, Figure 4D) case. The graphs reveal several key observations in agreement with the experiments: (1) condensation grows faster and reaches a larger height close to the neck where the distance to the droplet is minimal. In contrast, condensation height remains small close to the central dimple due to the greater distance. (2) In the bouncing case, condensation height saturates, as its evolution nearly stops. This behavior is also visible in the bouncing case at finite ΔT (Video S2). Finally, the model also provides the corresponding time evolution of ΔT_{dyn} in bouncing (Figure 4E) and non-bouncing (Figure 4F) cases, which helps clarify what limits condensation. Near the neck, the strong heat flux rapidly raises the lubricant layer temperature; hence, ΔT_{dyn} vanishes to 0°C . This halts the condensation, limits its total height, and allows bouncing to occur. Once the drop reaches its maximum extension, the temperature difference almost completely disappears, which explains why, experimentally, rupture of the air layer never occurs during the retracting phase.

Minimal scaling model for condensation-driven air-film rupture

To get a better understanding of the bouncing failure due to condensation, we propose a minimal model. We start by considering the heat flux through the air layer. The ratio of its diffusive latent part to its conductive contribution is written as a gas-phase evaporative cooling number $E_c = L_v D \Delta c_{\text{sat}} / \lambda_a \Delta T$.⁴⁴ For water with $T_o = 25^\circ\text{C}$, E_c is a growing function of ΔT with a value at $\Delta T = 0^\circ\text{C}$ of 2.7 larger than 1. Hence, we only consider the diffusive latent heat flux in the air layer, which neglects the condensation height $h \ll H$, written as $L_v D \Delta c_{\text{sat}} / H$. We further simplify its expression with a first-order Taylor expansion in ΔT_{dyn} of Δc_{sat} : $L_v D (\partial \Delta c_{\text{sat}} / \partial \Delta T) \Delta T_{\text{dyn}} / H$, where we remind

readers that $\Delta T_{\text{dyn}} = T_{W,S} - T_{L,S}$. The heat flux continuity at the drop/air/lubricant interface is then written as

$$\lambda_W \frac{T_W - T_{W,S}}{\sqrt{\alpha_W t}} \approx L_v D \frac{\partial \Delta c_{\text{sat}}}{\partial \Delta T} \frac{T_{W,S} - T_{L,S}}{H} \approx \lambda_L \frac{T_{L,S} - T_o}{\sqrt{\alpha_L t}}. \quad (\text{Equation 2})$$

This relation can be interpreted in terms of a thermal-circuit analogy. The latent heat transport across the vapor gap defines an effective thermal resistance $R_{\text{lat}} = H / (L_v D (\partial \Delta c_{\text{sat}} / \partial \Delta T))$, while the drop and lubricant are associated with transient thermal resistances $R_W = t^{1/2} / e_W$, $R_L = t^{1/2} / e_L$, where $e_W = \sqrt{\rho C_W \lambda_W}$ and $e_L = \sqrt{\rho_L C_L \lambda_L}$ are the thermal effusivities of the drop and lubricant, respectively. Equation 2 therefore describes three thermal resistances in series, so that the dynamic temperature drops across the vapor gap is written as

$$\frac{\Delta T_{\text{dyn}}}{\Delta T} = \frac{1}{1 + (R_W + R_L) / R_{\text{lat}}}.$$

Making the time evolution explicit, we obtain

$$\frac{\Delta T_{\text{dyn}}}{\Delta T} \approx \frac{1}{1 + (t / \tau_{th})^{1/2}},$$

where τ_{th} is the thermal coupling time, defined as

$$\tau_{th} = \left(\frac{H}{L_v D \frac{\partial \Delta c_{\text{sat}}}{\partial \Delta T} \left(\frac{1}{e_L} + \frac{1}{e_W} \right)} \right)^2.$$

τ_{th} represents the time at which the combined thermal resistance of the drop and lubricant overcomes the effective thermal resistance associated with latent heat transport across the vapor gap. For $t \ll \tau_{th}$, $R_W + R_L \ll R_{\text{lat}}$, so that most of the temperature drop is localized across the vapor gap and $\Delta T_{\text{dyn}} \approx \Delta T$. By contrast, for $t \gg \tau_{th}$, the liquid-side resistance becomes significant, causing the drop-side interface to cool and the lubricant-side interface to warm, thereby progressively reducing ΔT_{dyn} . More generally, this also shows that the less effusive liquid sets the dominant liquid-side thermal resistance. Here, $e_W / e_L \approx 3$, so that the water contribution to the thermal resistance is small compared to that of the lubricant, but to maintain the generality of the model, we retain both contributions.

We now describe the diffusion-limited condensation growth. Neglecting again $h \ll H$, the condensation height scales as

$$h \approx a \frac{D}{\rho H} \frac{\partial \Delta c_{\text{sat}}}{\partial \Delta T} \Delta T_{\text{dyn}} t, \quad (\text{Equation 3})$$

where a is an adjustable dimensionless prefactor similar to that of Equation 1, accounting for geometrical and morphological effects not captured by this 1D scaling model, such as the shape of condensation drops forming liquid lenses on the lubricant layer. Introducing the characteristic condensation time $\tau_c = \frac{\rho H^2}{D \frac{\partial \Delta c_{\text{sat}}}{\partial \Delta T} \Delta T}$, and using Equation 3 the condensation height normalized by the vapor gap thickness H is written as

$$\frac{h}{H} \approx a \frac{t / \tau_c}{1 + (t / \tau_{th})^{1/2}}. \quad (\text{Equation 4})$$

This equation for the condensation dynamics involves two characteristic timescales: the condensation time τ_c , associated with gap filling under a fixed driving ΔT , and the thermal coupling time τ_{th} , associated with the buildup of surface heating in the lubricant. Their relative magnitude determines the dominant growth regime. At $t \sim \tau_{th}$, Equation 4 gives $h/H \sim \tau_{th}/\tau_c$, so that τ_{th}/τ_c directly quantifies how much condensate has formed when thermal coupling sets in. If $\tau_{th} \gg \tau_c$, condensation remains essentially in the linear regime $h/H \sim t/\tau_c$. By contrast, if $\tau_{th} \ll \tau_c$, thermal coupling becomes important while $h \ll H$, and growth is dominated by the thermally limited regime $h/H \sim \sqrt{t\tau_{th}}/\tau_c$. Although both τ_{th} and τ_c scale with the vapor-gap thickness H , their ratio τ_{th}/τ_c is independent of H . In our experiments, τ_{th}/τ_c always remains much smaller than unity, with a maximum value of about 0.1 reached at $\Delta T = 60^\circ\text{C}$. Therefore, the initial linear regime can be neglected, and Equation 4 then reduces to

$$h \approx a \frac{\sqrt{t}}{\rho L_v \left(\frac{1}{e_L} + \frac{1}{e_W} \right)} \Delta T. \quad (\text{Equation 5})$$

We now focus on finding a description of the transition velocity $V_c(\Delta T)$ from bouncing to no bouncing. The transition occurs when the condensation height reaches the minimum thickness of the air film h_{\min} , in a time shorter than the bouncing time τ , that is, for $h(\tau) = h_{\min}$. Using $\tau \sim (\rho R^3/\gamma)^{1/228,36}$ for the bouncing time and the scaling derived by Mandre et al.⁴⁵ and Mani et al.⁴⁶ for h_{\min} , which writes $h_{\min} \approx 2.54 R St^{-8/9} We^{-2/3}$, where $St = \rho VR/\eta_a$ is the Stokes number and η_a is the air viscosity. Using Equation 5, we obtain an explicit equation for the transition velocity V_c :

$$V_c \approx \left(\frac{2.54}{a} \right)^{\frac{9}{20}} L_v^{\frac{9}{20}} \left(\frac{1}{e_L} + \frac{1}{e_W} \right)^{\frac{9}{20}} \rho^{-\frac{29}{80}} R^{-\frac{47}{80}} \gamma^{\frac{33}{80}} \eta_a^{\frac{2}{5}} \frac{1}{\Delta T^{\frac{9}{20}}}. \quad (\text{Equation 6})$$

The model is shown in blue in Figure 4B and adjusted to the experimental data by setting its sole free parameter $a = 0.309$. The plot reveals that the bouncing/spreading transition is remarkably well described by Equation 6 despite substantial simplifications. The model also shows that the critical velocity varies with $V_c \sim 1/\Delta T^{9/20}$. Interestingly, if we ignore the thermal effects ($\tau_{th} \gg \tau_c$), the typical condensation height h reached after a time τ is written as $h \sim (D(\partial \Delta c_{\text{sat}}/\partial \Delta T) \Delta T \tau / \rho)^{1/2}$, and setting the transition to $h \sim h_{\min} \sim 1/V_c^{20/9}$ gives $V_c \sim 1/\Delta T^{9/40}$, a slight decrease that does not well describe the observed transition.

We explored the border of the transition regime by setting $t = \tau$ and now test our model on the rupture time. The drop should start spreading on the surface at a time t_r such that $h(t_r) = h_{\min}$; using Equation 5, we find

$$t_r \approx \left(\frac{1}{e_L} + \frac{1}{e_W} \right)^2 \left(\frac{\rho L_v h_{\min}}{a} \right)^2 \frac{1}{\Delta T^2},$$

and with $h_{\min} \approx 2.54 R St^{-8/9} We^{-2/3}$,^{45,46} we obtain

$$t_r \approx \left(\frac{2.54}{a} \right)^2 L_v^2 \left(\frac{1}{e_L} + \frac{1}{e_W} \right)^2 (\rho R)^{-\frac{10}{9}} \eta_a^{\frac{16}{9}} \gamma^{\frac{4}{9}} \frac{1}{V_c^{\frac{40}{9}} \Delta T^2}. \quad (\text{Equation 7})$$

Using the value previously obtained for a , we plot Equation 7 in blue on the rupture time plot in Figure 2D. We again find excellent agreement, which further demonstrates that this simplified model robustly and quantitatively predicts the bouncing-to-spreading transition. While smaller lubricant thicknesses are difficult to achieve reproducibly without introducing surface texture, we also test larger lubricant thicknesses, $h_o = 14 \pm 1$ and $20 \pm 2 \mu\text{m}$, and observe no measurable change in the rupture dynamics compared with the reference case $h_o = 8 \pm 1 \mu\text{m}$ (Figure S5). This is expected from the thermal model, as heat penetrates the lubricant over a diffusion length $\delta_L \sim (\alpha_L t)^{1/2}$, which is on the order of $10 \mu\text{m}$ over the millisecond rupture times measured here. Therefore, once h_o exceeds δ_L , the rupture dynamics should become only weakly sensitive to the total lubricant thickness, whereas for $h_o < \delta_L$, the underlying substrate is expected to contribute through an effective liquid-side effusivity.

DISCUSSION

We demonstrated that air-film-mediated bouncing on lubricated surfaces depends on the liquid volatility and the temperature difference with the substrate. For hot volatile liquids such as water, condensation forms on the substrate, which generates a liquid roughness triggering contact with the drop interface. The contact point depends on the minimum thickness of the air layer, which decreases with the impact velocity. As a result, the critical temperature for bouncing failure depends on impact velocity. This differs from superhydrophobic surfaces, where the condensation time is governed by the surface structure height,^{20,21} yielding a critical temperature that is essentially independent of impact velocity. Importantly, the condensation dynamics, hence the bouncing threshold, is dominated by heat transfer in the least effusive material between the drop and the substrate, which offers a possibility to tune the bouncing/spreading transition via the substrate thermal properties. The experiments also revealed interesting condensation patterns on the lubricant layer with elongated droplets near the edge of the impact zone. Our model shows that there is a large temperature gradient close to the drop edge, as the temperature near the center rapidly increases while the edge is still at room temperature T_o . This creates a surface tension gradient $d\gamma/dx \sim \Gamma \Delta T/L$ and Marangoni flow, which elongates the condensed drops. Balancing this gradient by the viscous stress across the drop thickness h , $\eta(L/t)/h$, gives the extension of the drops $L \sim (\Gamma h \Delta T t / \eta)^{1/2}$. Taking $h \sim 100 \text{ nm}$, $\Delta T = 50^\circ\text{C}$, and $t = 1 \text{ ms}$ for the typical time over which the drop elongates, we find $L \sim 500 \mu\text{m}$ in good qualitative agreement with images from Figures 2B and 2C. Finally, we discuss the applicability of our model to volatile liquids other than water. Our model in Equation 5 is obtained by neglecting the conductive part of the heat flux in the air layer ($E_c \gg 1$) and by considering that the thermal couplings become important before any significant condensation growth ($\tau_{th} \ll \tau_c$). For common volatile liquids such as isopropyl alcohol, ethanol, acetone, or benzene (see Note S4), the two approximations remain valid, so our model applies. The only parameter that should depend on the solvent is coefficient a in Equation 1, which quantifies how the geometry of the condensed droplets modifies the surface deformation. For water droplets on a silicone oil layer, a should result from a

Table 1. Silicone oil spin-coating parameters

h_o (μm)	Step 1	Step 2
8 ± 1	10 s, 500 rpm	60 s, 1,000 rpm
14 ± 1	10 s, 300 rpm	45 s, 650 rpm
20 ± 2	10 s, 250 rpm	40 s, 500 rpm

complex dynamic process involving condensation, cloaking, and engulfment of water nuclei into the silicone oil.⁴⁷ This dynamical process is consistent with post-condensation focused ion beam (FIB) observations by Anand et al.⁴⁸ and is expected to be affected by the lubricant's viscosity in a non-trivial way. More viscous lubricants may slow down the cloaking dynamics of the nuclei and their subsequent engulfment, as well as water diffusion through the viscous silicone oil.⁴⁹ These coupled condensation dynamics remain an open question, but resolving them directly is experimentally challenging because of the short temporal and small spatial scales involved. The macroscopic dependence of a on viscosity could therefore provide an indirect way to probe these dynamics. For the case of solvents that do not engulf in the lubricant and instead form liquid lenses at the surface, a should be larger, and viscosity may still play a role through cloaking, diffusion, and liquid lens formation. Finally, we expect a to be even larger on solids that cannot deform. This provides a potential route to tune the surface response to hot liquid. In particular, it would be interesting to consider lubricants that are perfectly wetted by the impacting liquid. In such systems, filmwise condensation may produce a sufficiently flat film for bouncing to persist. Beyond their fundamental interest, our results offer insights for applications where drop bouncing plays a critical role. In agriculture, suppressing the bounce of pesticides off leaves reduces environmental contamination and chemical waste. Similarly, in inkjet printing or spray coating applications, preventing rebound helps maintain print quality and coating uniformity. Our results suggest that, for such applications, increasing the temperature of the ejected liquid may be an effective way to prevent bouncing.

METHODS

Substrate preparation

Substrates are prepared using the method developed by Tenjim-bayashi et al.,³⁹ in which smooth glass substrates are modified with phenyl silane. This surface enables the stabilization of a thin layer of silicone oil terminated with a -OH group (X-22-170BX, ShinEtsu Chemical), which has a high affinity with the silane groups at the surface. The lubricant is deposited on the substrate with a micropipette and spin coated using the values displayed in Table 1. The mass difference Δm of the substrate before and after spin coating is measured with a precision balance (Shinko Denshi, Model XFR-225W, accuracy of 0.01 mg), and the lubricant thickness is estimated with $h_o = \Delta m / \rho_L S$, where S is the surface area of the substrate.

Saturated vapor concentration

The saturated vapor concentration of water $c_{\text{sat}}(T)$ is derived from Dalton's law: $c_{\text{sat}}(T) = \rho_{\text{air}}(M_w/M_{\text{air}})(P_{\text{sat}}(T)/P_o)$, where ρ_{air} is

the air density; M_w and M_{air} are the molar masses of water and air, respectively; $P_{\text{sat}}(T)$ is the saturated vapor pressure of water at temperature T ; and P_o is the atmospheric pressure. The saturated vapor pressure of water is estimated with the Rankine formula $P_{\text{sat}}(T) = P_o \exp(13.7 - 5,120/T)$, so that we obtain $c_{\text{sat}}(T) = \rho_{\text{air}}(M_w/M_{\text{air}}) \exp(13.7 - 5,120/T)$.

RESOURCE AVAILABILITY

Lead contact

Requests for further information and resources should be directed to and will be fulfilled by the lead contact, Timothée Mouterde (mouterde@g.ecc.u-tokyo.ac.jp).

Materials availability

This study did not generate new unique reagents.

Data and code availability

- All original code has been deposited at Zenodo and is publicly available at <https://doi.org/10.5281/zenodo.20187901> as of the date of publication.
- All data reported in this paper and any additional information required to reanalyze the data are available from the [lead contact](#) upon reasonable request.

ACKNOWLEDGMENTS

We thank Prof. Junichiro Shiomi and Prof. Yaerim Lee for allowing us to use their spin coater. We thank Mari Chikarashi for preliminary experiments. T.M. and M.T. acknowledge the financial support provided by the Japan Society for the Promotion of Science (JSPS) - Grant-in-Aid for Scientific Research (B), 24K01341. T.M. and P.K.R. gratefully acknowledge the financial support provided by the JSPS Grant-in-Aid for JSPS Fellows 23KF0106. M.T. appreciates support from WPI-MANA. G.D. acknowledges support from the Erasmus+ Program of the European Union.

AUTHOR CONTRIBUTIONS

Conceptualization, T.M. and M.T.; methodology, T.M.; investigation, T.M., G.D., S.T., Y.S., and P.K.R.; writing – original draft, T.M. and G.D.; writing – review & editing, T.M., M.T., and G.D.; funding acquisition, T.M., M.T., and P.K.R.; resources, T.M. and M.T.; supervision, T.M.

DECLARATION OF INTERESTS

The authors declare no competing interests.

DECLARATION OF GENERATIVE AI AND AI-ASSISTED TECHNOLOGIES IN THE WRITING PROCESS

During the preparation of this work, the authors used ChatGPT for language editing of the text. After using this tool or service, the authors reviewed and edited the content as needed and take full responsibility for the content of the publication.

SUPPLEMENTAL INFORMATION

Supplemental information can be found online at <https://doi.org/10.1016/j.newton.2026.100582>.

Received: August 26, 2025

Revised: April 2, 2026

Accepted: June 5, 2026

REFERENCES

- Josserand, C., and Thoroddsen, S.T. (2016). Drop Impact on a Solid Surface. *Annu. Rev. Fluid Mech.* 48, 365–391. <https://doi.org/10.1146/annurev-fluid-122414-034401>.
- Lohse, D. (2022). Fundamental fluid dynamics challenges in inkjet printing. *Annu. Rev. Fluid Mech.* 54, 349–382. <https://doi.org/10.1146/annurev-fluid-022321-114001>.
- Derby, B. (2010). Inkjet printing of functional and structural materials: Fluid property requirements, feature stability, and resolution. *Annu. Rev. Mater. Res.* 40, 395–414. <https://doi.org/10.1146/annurev-matsci-070909-104502>.
- Visser, C.W., Pohl, R., Sun, C., Römer, G.W., Huis in 't Veld, B., and Lohse, D. (2015). Toward 3D printing of pure metals by laser-induced forward transfer. *Adv. Mater.* 27, 4087–4092. <https://doi.org/10.1002/adma.201501058>.
- Damak, M., Hyder, M.N., and Varanasi, K.K. (2016). Enhancing droplet deposition through in-situ precipitation. *Nat. Commun.* 7, 12560. <https://doi.org/10.1038/ncomms12560>.
- Breitenbach, J., Roisman, I.V., and Tropea, C. (2018). From drop impact physics to spray cooling models: a critical review. *Exp. Fluids* 59, 55. <https://doi.org/10.1007/s00348-018-2514-3>.
- Dolovich, M.B., and Dhand, R. (2011). Aerosol drug delivery: developments in device design and clinical use. *Lancet* 377, 1032–1045. [https://doi.org/10.1016/S0140-6736\(10\)60926-9](https://doi.org/10.1016/S0140-6736(10)60926-9).
- Mishchenko, L., Hatton, B., Bahadur, V., Taylor, J.A., Krupenkin, T., and Aizenberg, J. (2010). Design of ice-free nanostructured surfaces based on repulsion of impacting water droplets. *ACS Nano* 4, 7699–7707. <https://doi.org/10.1021/nn102557p>.
- Yarin, A.L. (2006). Drop impact dynamics: splashing, spreading, receding, bouncing. *Annu. Rev. Fluid Mech.* 38, 159–192. <https://doi.org/10.1146/annurev-fluid.38.050304.092144>.
- Sprittles, J.E. (2024). Gas microfilms in droplet dynamics: When do drops bounce? *Annu. Rev. Fluid Mech.* 56, 91–118. <https://doi.org/10.1146/annurev-fluid-121021-021121>.
- Rioboo, R., Tropea, C., and Marengo, M. (2001). Outcomes from a drop impact on solid surfaces. *Atomiz. Spr.* 11, 12–165. <https://doi.org/10.1615/AtomizSpr.v11.i2.40>.
- Stow, C.D., and Hadfield, M.G. (1981). An experimental investigation of fluid flow resulting from the impact of a water drop with an unyielding dry surface. *Proc. R. Soc. London Ser. A* 373, 419–441. <https://doi.org/10.1098/rspa.1981.0002>.
- Mundo, C., Sommerfeld, M., and Tropea, C. (1995). Droplet-wall collisions: experimental studies of the deformation and breakup process. *Int. J. Multiph. Flow* 21, 151–173. [https://doi.org/10.1016/0301-9322\(94\)00069-V](https://doi.org/10.1016/0301-9322(94)00069-V).
- Villermaux, E., and Bossa, B. (2011). Drop fragmentation on impact. *J. Fluid Mech.* 668, 412–435. <https://doi.org/10.1017/S002211201000474X>.
- Bartolo, D., Josserand, C., and Bonn, D. (2006). Singular jets and bubbles in drop impact. *Phys. Rev. Lett.* 96, 124501. <https://doi.org/10.1103/PhysRevLett.96.124501>.
- Renardy, Y., Popinet, S., Duchemin, L., Renardy, M., Zaleski, S., Josserand, C., Drumright-Clarke, M.A., RICHARD, D., CLANET, C., and QUÉRÉ, D. (2003). Pyramidal and toroidal water drops after impact on a solid surface. *J. Fluid Mech.* 484, 69–83. <https://doi.org/10.1017/S0022112003004142>.
- Chandra, S., and Avedisian, C.T. (1991). On the collision of a droplet with a solid surface. *Proc. R. Soc. London Ser. A* 432, 13–41. <https://doi.org/10.1098/rspa.1991.0002>.
- Thoroddsen, S.T., and Sakakibara, J. (1998). Evolution of the fingering pattern of an impacting drop. *Phys. Fluids* 10, 1359–1374. <https://doi.org/10.1063/1.869661>.
- Richard, D., and Quéré, D. (2000). Bouncing water drops. *Europhys. Lett.* 50, 769–775. <https://doi.org/10.1209/epl/12000-00547-6>.
- Mouterde, T., Lecointre, P., Lehoucq, G., Checco, A., Clanet, C., and Quéré, D. (2019). Two recipes for repelling hot water. *Nat. Commun.* 10, 1410. <https://doi.org/10.1038/s41467-019-09456-8>.
- Zhu, P., Chen, R., and Wang, L. (2019). Topography-directed hot-water super-repellent surfaces. *Adv. Sci.* 6, 1900798. <https://doi.org/10.1002/adv.201900798>.
- Shiri, S., Murrizi, A., and Bird, J.C. (2018). Trapping a hot drop on a superhydrophobic surface with rapid condensation or microtexture melting. *Micromachines* 9, 566. <https://doi.org/10.3390/mi9110566>.
- Jung, S., Tiwari, M.K., Doan, N.V., and Poulikakos, D. (2012). Mechanism of supercooled droplet freezing on surfaces. *Nat. Commun.* 3, 615. <https://doi.org/10.1038/ncomms1630>.
- Wang, H., Wu, Q., Okagaki, J., Alizadeh, A., Shamim, J.A., Hsu, W.L., and Daiguji, H. (2021). Bouncing behavior of a water droplet on a superhydrophobic surface near freezing temperatures. *Int. J. Heat Mass Transf.* 174, 121304. <https://doi.org/10.1016/j.ijheatmasstransfer.2021.121304>.
- de Ruiter, J., Soto, D., and Varanasi, K.K. (2018). Self-peeling of impacting droplets. *Nat. Phys.* 14, 35–39. <https://doi.org/10.1038/nphys4252>.
- Liu, Y., Zheng, Y., Zhou, Y., Zhao, W., Li, Y., Tang, S., Wang, C., Wang, S., Chai, Y., and Zhu, P. (2025). Self-lubricated bouncing of hot droplets. *Newton* 1, 100014. <https://doi.org/10.1016/j.newton.2025.100014>.
- Shiri, S., and Bird, J.C. (2017). Heat exchange between a bouncing drop and a superhydrophobic substrate. *Proc. Natl. Acad. Sci. USA* 114, 6930–6935. <https://doi.org/10.1073/pnas.1700197114>.
- Richard, D., Clanet, C., and Quéré, D. (2002). Contact time of a bouncing drop. *Nature* 417, 811. <https://doi.org/10.1038/417811a>.
- Bird, J.C., Dhiman, R., Kwon, H.M., and Varanasi, K.K. (2013). Reducing the contact time of a bouncing drop. *Nature* 503, 385–388. <https://doi.org/10.1038/nature12740>.
- Gauthier, A., Symon, S., Clanet, C., and Quéré, D. (2015). Water impacting on superhydrophobic macrotextures. *Nat. Commun.* 6, 8001. <https://doi.org/10.1038/ncomms9001>.
- Liu, Y., Moevius, L., Xu, X., Qian, T., Yeomans, J.M., and Wang, Z. (2014). Pancake bouncing on superhydrophobic surfaces. *Nat. Phys.* 10, 515–519. <https://doi.org/10.1038/nphys2980>.
- Kolinski, J.M., Mahadevan, L., and Rubinstein, S.M. (2014). Drops can bounce from perfectly hydrophilic surfaces. *Europhys. Lett.* 108, 24001. <https://doi.org/10.1209/0295-5075/108/24001>.
- de Ruiter, J., Lagraauw, R., Van Den Ende, D., and Mugele, F. (2015). Wettability-independent bouncing on flat surfaces mediated by thin air films. *Nat. Phys.* 11, 48–53. <https://doi.org/10.1038/nphys3145>.
- Zhang, L., Soori, T., Rokoni, A., Kaminski, A., and Sun, Y. (2021). Air film contact modes of drop impact on lubricated surfaces under reduced pressures. *Phys. Fluids* 33, 092110. <https://doi.org/10.1063/5.0065747>.
- Chubynsky, M.V., Belousov, K.I., Lockerby, D.A., and Sprittles, J.E. (2020). Bouncing off the walls: the influence of gas-kinetic and van der Waals effects in drop impact. *Phys. Rev. Lett.* 124, 084501. <https://doi.org/10.1103/PhysRevLett.124.084501>.
- Hao, C., Li, J., Liu, Y., Zhou, X., Liu, Y., Liu, R., Che, L., Zhou, W., Sun, D., Li, L., et al. (2015). Superhydrophobic-like tunable droplet bouncing on slippery liquid interfaces. *Nat. Commun.* 6, 7986. <https://doi.org/10.1038/ncomms8986>.
- Lo, H.Y., Liu, Y., and Xu, L. (2017). Mechanism of contact between a droplet and an atomically smooth substrate. *Phys. Rev. X* 7, 021036. <https://doi.org/10.1103/PhysRevX.7.021036>.
- Pack, M., Hu, H., Kim, D., Zheng, Z., Stone, H.A., and Sun, Y. (2017). Failure mechanisms of air entrainment in drop impact on lubricated surfaces. *Soft Matter* 13, 2402–2409. <https://doi.org/10.1039/C7SM00117G>.
- Tenjimbayashi, M., Togasawa, R., Manabe, K., Matsubayashi, T., Moriya, T., Komine, M., and Shiratori, S. (2016). Liquid-infused smooth coating

- p>with transparency, super-durability, and extraordinary hydrophobicity.
- Adv. Funct. Mater.*
- 26, 6693–6702.
- <https://doi.org/10.1002/adfm.201602546>
- .
40. Sharma, P.K., and Dixit, H.N. (2021). Regimes of wettability-dependent and wettability-independent bouncing of a drop on a solid surface. *J. Fluid Mech.* 908, A37. <https://doi.org/10.1017/jfm.2020.773>.
41. Geri, M., Keshavarz, B., McKinley, G.H., and Bush, J.W.M. (2017). Thermal delay of drop coalescence. *J. Fluid Mech.* 833, R3. <https://doi.org/10.1017/jfm.2017.686>.
42. Popinet, S. (2018). Numerical models of surface tension. *Annu. Rev. Fluid Mech.* 50, 49–75. <https://doi.org/10.1146/annurev-fluid-122316-045034>.
43. Popinet, S. (2019). Basilisk flow solver and PDE library. Available at: <http://basilisk.fr>
44. Xu, X., and Ma, L. (2015). Analysis of the effects of evaporative cooling on the evaporation of liquid droplets using a combined field approach. *Sci. Rep.* 5, 8614. <https://doi.org/10.1038/srep08614>.
45. Mandre, S., Mani, M., and Brenner, M.P. (2009). Precursors to splashing of liquid droplets on a solid surface. *Phys. Rev. Lett.* 102, 134502. <https://doi.org/10.1103/PhysRevLett.102.134502>.
46. Mani, M., Mandre, S., and Brenner, M.P. (2010). Events before droplet splashing on a solid surface. *J. Fluid Mech.* 647, 163–185. <https://doi.org/10.1017/S0022112009993594>.
47. Cuttle, C., Thompson, A.B., Pihler-Puzović, D., and Juel, A. (2021). The engulfment of aqueous droplets on perfectly wetting oil layers. *J. Fluid Mech.* 915, A66. <https://doi.org/10.1017/jfm.2021.90>.
48. Anand, S., Rykaczewski, K., Subramanyam, S.B., Beysens, D., and Varanasi, K.K. (2015). How droplets nucleate and grow on liquids and liquid impregnated surfaces. *Soft Matter* 11, 69–80. <https://doi.org/10.1039/c4sm01424c>.
49. Ge, Q., Raza, A., Li, H., Sett, S., Miljkovic, N., and Zhang, T. (2020). Condensation of satellite droplets on lubricant-cloaked droplets. *ACS Appl. Mater. Interfaces* 12, 22246–22255. <https://doi.org/10.1021/ac-sami.9b22417>.